PAPER

Check for updates

Hydrogen evolution reaction mechanisms in thiosemicarbazone metal complexes: a combined theoretical and experimental investigation on the impact of proton source†

Jana Mehrez, Alexandre Barrozo, [ID] Léa Delmotte, Renaud Hardré, [ID]
Michael Papadakis* and Maylis Orio [ID] *

In the pursuit of developping efficient and green methods for hydrogen production, a key focus is the development of the most energy-efficient catalysts. The analysis of various proton sources primarily aims at eliminating rate-limiting steps associated with protonation events and ensuring the stability of the catalyst. In this work, we report how two distinct proton sources can cause a mechanistic shift in the hydrogen evolution reaction. Specifically, we explore this reactivity change in the presence of triethylammonium and trifluoroacetic acid with two thiosemicarbazone-based complexes, using cobalt and nickel metal centers. Our combined experimental and theoretical results reveal that the complete sequence of steps leading to hydrogen release strongly depends on the proton source. This demonstrates the importance of thoroughly investigating the interactions between a catalyst and a proton source to optimize hydrogen evolution systems.

Introduction

With the increasing prominence of hydrogen as a key fuel source, the development of new catalysts able to perform the hydrogen evolution reaction (HER) continue to advance. Most of the focus has been put on molecules that either mimic the structure or the function of hydrogenases.[1–13] However, the choice of proton sources is a rather overlooked area of study. Discussions often focus on finding acids that are strong enough to ensure that proton transfer does not become the rate-limiting step, while still maintaining the stability of the catalyst.[14] Different proton sources, such as triethylammonium (Et_3NH^+) and trifluoroacetic acid (TFA) will interact with catalysts in different ways, leading to multiple hydrogen-bond interactions that can result in proton transfers to distinct protonation sites. Furthermore, it is worth noting that, as the redox state of the catalyst changes during the HER process, the proton affinities of each potential protonation site also evolve. Considering HER involves more than a single electrochemical event, the pK_a of the proton source and the catalyst's nature can influence the sequence and location of proton transfer

steps. This versatility can lead to different catalytic cycles, depending on the specific conditions at play.

We have recently reported comprehensive experimental and theoretical studies investigating the mechanisms of homogeneous HER catalysts based on non-innocent thiosemicarbazone (TSC) ligands which can actively participate in the catalytic process by storing both electrons and protons.[15–22] These studies focused on a Ni-based TSC complex (**NiTSC-OCH₃**) in the presence of trifluoroacetic acid (TFA),[19,21,22] and an analogous Co-based complex (**CoTSC-OCH₃**) using triethylammonium (Et_3NH^+).[20,23] In these studies, the nature of both the metal centre and the proton source differs, resulting in distinct reaction pathways. Interestingly, our complementary study on a series Ni-based complexes explored how chemical modifications to the non-innocent TSC ligand might influence the reaction pathway, considering three substituents of different electron-donating abilities placed at the *para* position on the phenyl rings.[21] Our findings indicated that these changes had no significant impact on the catalytic cycle and only affected the HER catalysis parameters.[24] However, the precise factors responsible for the variations in catalytic performance remain unclear. Consequently, further exploration was needed to unravel how parameters such as electronic properties of the metal, proton transfer dynamics, and ligand interactions contribute to the observed mechanistic discrepancies and influence the overall efficiency of the catalysts in the HER process. In this work, we aimed to conduct a more in-

Aix-Marseille Univ, CNRS, Centrale Med, iSm2, Marseille, France.
E-mail: michail.papadakis@univ-amu.fr, maylis.orio@univ-amu.fr
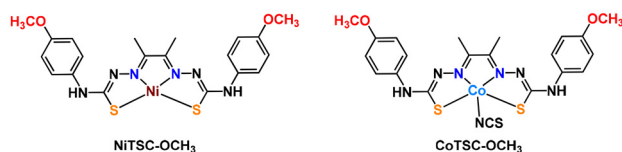
Scheme 1 Structures of nickel and cobalt thiosemicarbazone complexes considered in this work.

depth comparison between two TSC metal-based catalysts, namely **NiTSC-OCH₃** and **CoTSC-OCH₃** (Scheme 1) by examining their behavior using TFA and Et₃NH⁺ as proton sources.

Our study reveals that the catalytic mechanism can shift depending on the choice of acid. While it is usually assumed that a stronger proton source will enhance HER catalytic performance by facilitating proton transfer, our results indicate that the interaction between the acid and the catalyst is more nuanced, with different acid-catalyst pairs leading to distinct catalytic pathways. This is an important finding, as any attempt to optimize a given catalyst needs now to account for its exact interaction with the acid and distinct rate-limiting steps.

Results and discussion

### Synthesis and characterization

Syntheses of complexes **NiTSC-OCH₃**, **CoTSC-OCH₃** and Et₃NHBF₄ salt were performed following protocols previously reported in literature.[22,25,26]

Electrocatalytic studies and benchmarking of performances

Cyclic voltammograms (CV) in catalytic conditions were recorded using experimental conditions similar to those employed in our previously reported studies for electrocatalytic proton reduction combining **NiTSC-OCH₃** with trifluoroacetic acid (TFA)[19] and **CoTSC-OCH₃** with triethylammonium tetrafluoroborate (Et₃NHBF₄).[20] In this work, we considered switching proton sources for each complex to investigate the reactivity of **NiTSC-OCH₃** with Et₃NHBF₄ and that of **CoTSC-OCH₃** with TFA. The redox behaviour of the complexes was first investigated in the potential range between 0 and −2.6 V *vs.* Fc⁺/⁰. The experiments were performed at room temperature, with a glassy carbon electrode in a nitrogen-purged anhydrous DMF solution, containing tetrabutylammonium hexafluorophosphate (NBu₄PF₆) as a supporting electrolyte. In the absence of acid, two quasi-reversible processes are detected in the cathodic region for both complexes (Table 1).

To study the capability of the two complexes to mediate proton reduction catalysis, we recorded their cyclic voltammograms under nitrogen in the presence of a proton source using TFA (pK_a = 6.0 in DMF)[27] with **CoTSC-OCH₃** and Et₃NHBF₄ (pK_a = 9.2 in DMF)[14] with **NiTSC-OCH₃** (Fig. 1 and S1†). Focusing on the cobalt complex with TFA, the addition of acid triggers the appearance of three irreversible waves indicative of potential-dependent mechanisms and consistent with previous observations for **NiTSC-OCH₃** with TFA. The first wave displays a peak potential at −1.42 V *vs.* Fc⁺/⁰ while the peak potential of the next two waves are shifted to more negative values upon successive additions of TFA (from −1.79 to −1.89 V, and from −2.09 to −2.37 V *vs.* Fc⁺/⁰, with 10 and 60 mM of acid, respectively). The mid-wave potential of the process occurring at more positive potentials is of −1.28 V *vs.* Fc⁺/⁰ and its intensity is correlated with acid concentration in the solution (Fig. S2†). A different response in current is obtained for **NiTSC-OCH₃** in the presence of Et₃NH⁺ with the appearance of two irreversible waves upon acid addition (Fig. S2†). The first wave with a peak potential at −1.65 V *vs.* Fc⁺/⁰ is mostly unaffected when raising acid concentration, while the second one slightly shifts with increasing amounts of Et₃NH⁺ (from −2.28 to −2.42 V *vs.* Fc⁺/⁰ with 20 and 100 mM of acid, respectively). This catalytic wave displays a mid-wave potential of −2.08 V *vs.* Fc⁺/⁰ with a current response proportional to acid concentration.
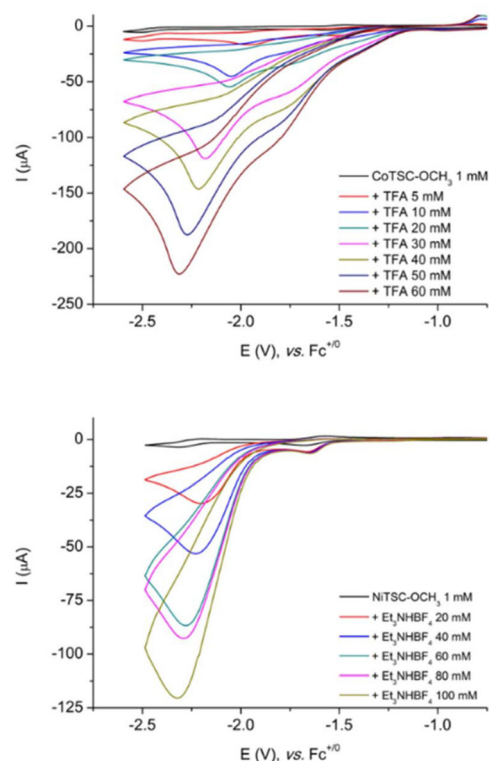
Fig. 1 Successive cyclic voltammograms of a DMF solution (0.1 M NBu₄PF₆) with 1 mM of (top) **CoTSC-OCH₃** in the presence of increasing amounts of TFA and (bottom) **NiTSC-OCH₃** in the presence of increasing amounts of Et₃NHBF₄. Scan rate 500 mV s⁻¹ using a glassy carbon working electrode.

Table 1 Electrochemical data for Ni- and Co-TSC-OCH₃ complexes (V *vs.* Fc⁺/⁰)[19,20]

Complex	$E°$ 1ˢᵗ reduction	$E°$ 2ⁿᵈ reduction	$E°$ 3ʳᵈ reduction
CoTSC-OCH₃	−0.60	−1.48	−2.48
NiTSC-OCH₃	−1.57	−2.20	—

Dip and rinse tests were performed to confirm that the current response observed upon adding a proton source was not due to the absorption of any species on the electrode surface.

After each measurement, the working electrode was transferred to a fresh DMF solution (0.1 M NBu$_4$PF$_6$). Following the addition of either TFA or Et$_3$NH$^+$, no catalytic wave was recorded, confirming that these systems are homogeneous in nature (Fig. S3†). To confirm that the observed catalytic waves resulted from the electrocatalytic reduction of protons into hydrogen, bulk electrolysis experiments were conducted alongside gas analysis.

Solutions were prepared in 8 mL of DMF (0.1 M NBu$_4$PF$_6$) containing 1 mM of each complex. For **NiTSC-OCH$_3$**, 100 mM of Et$_3$NH$^+$ was added, while for **CoTSC-OCH$_3$**, 60 mM of TFA was used to match the conditions of our previous reported works. Continuous in-line GC analysis was used to monitor the gas products from each reaction. A mercury pool working electrode was employed to ensure that any nanoparticle formed during the catalysis would be absorbed into the mercury, thereby maintaining the systems' homogeneity.

For the cobalt catalyst with TFA, bulk electrolysis experiments were performed by applying a controlled potential of −1.6 V $vs.$ Fc$^{+/0}$ for 16 hours and the complex demonstrated catalytic activity for proton reduction (Fig. 2 and S4†).

Both catalysts produce hydrogen with TFA using similar applied potential values (−1.6 and −1.7 V $vs.$ Fc$^{+/0}$ for **CoTSC-OCH$_3$** and **NiTSC-OCH$_3$** respectively). While the turnover frequency (TOF) of **CoTSC-OCH$_3$** is higher at early-stage catalysis (96 s^{-1} $vs.$ 11 s^{-1} for **NiTSC-OCH$_3$**), they eventually yield fairly similar TOF values after 16 h of catalysis (117 and 90 s^{-1}, respectively). However, the cobalt complex provides enhanced H$_2$ production compared to the nickel analogue with higher turnover number (TON) and faradaic yield (FY, 35 and 88% $vs.$ 21 and 80% for **NiTSC-OCH$_3$**, Tables S1 and S2†) and displays a decreased overpotential value, η (0.294 V $vs.$ 0.344 V for **NiTSC-OCH$_3$**, Table S3†).[19]

For the nickel catalyst with Et$_3$NH$^+$, measurements were performed at a fixed potential of −2.1 V $vs.$ Fc$^{+/0}$ over 4 hours (Fig. 2 and S5†). Comparing the catalytic performances of the two complexes with Et$_3$NH$^+$, the Co complex significantly outperforms the Ni analogue in every aspect. Indeed, **CoTSC-OCH$_3$** mediates proton reduction into hydrogen at a lower applied potential (−1.6 V $vs.$ −2.1 V $vs.$ Fc$^{+/0}$ for **NiTSC-OCH$_3$**) to provide increased FY (65 $vs.$ 58% for **NiTSC-OCH$_3$**) and TON (9 $vs.$ 2 for **NiTSC-OCH$_3$**) leading to a higher efficiency with an enhanced TOF value (130 s^{-1} $vs.$ 24 s^{-1} for **NiTSC-OCH$_3$**) and a lower overpotential requirement (0.311 V $vs.$ 0.908 V for **NiTSC-OCH$_3$**, Tables S1–S3†).[20] For both proton source, the cobalt-based TSC complex seems to be a better catalyst for hydrogen evolution that its nickel counterpart. However, the mechanistic implications of the proton source strength cannot be firmly established based only on the current set of experimental data. The main insight we can get originates from the UV-vis data of the complexes recorded both in the presence and absence of proton sources. Considering no change is observed in the spectral signatures
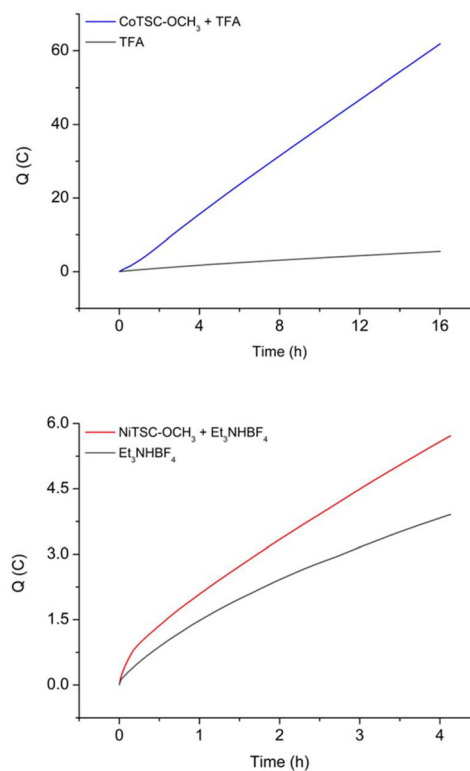
Fig. 2 Coulometry of **CoTSC-OCH$_3$** with 60 mM TFA during bulk electrolysis experiment at −1.6 V $vs.$ Fc$^{+/0}$ (top blue line) and blank experiment of 60 mM TFA in the absence of **CoTSC-OCH$_3$** (top grey line) and **NiTSC-OCH$_3$** with 100 mM Et$_3$NHBF$_4$ during bulk electrolysis experiment at −2.1 v $vs.$ Fc$^{+/0}$ (bottom red line) and blank experiment of 100 mM Et$_3$NH$^+$ in the absence of **NiTSC-OCH$_3$** (bottom grey line). The electrolytic solutions contain 0.1 M NBu$_4$PF$_6$ in DMF and 1 mM of each complex. Bulk electrolysis experiments were performed using a mercury pool working electrode.

with and without acid (Fig. S6†), these data indeed support our previous analysis suggesting that the reaction mechanisms involving our nickel and cobalt complexes do not involve an initial protonation step.[22–24]

To better understand how acid strength influences the HER pathway, we have conducted an extensive theoretical investigation of the possible catalytic cycles involving **CoTSC-OCH$_3$** and **NiTSC-OCH$_3$** using density functional theory (DFT) calculations. Our computational studies will allow us to probe the reaction energetics of both thiosemicarbazone metal-based complexes in the presence of each proton source, providing valuable insights into the underlying mechanistic differences. Through theoretical modelling of the reaction pathways, we aim at identifying key steps in the catalytic cycle where the proton source could have significant effect.

DFT Calculations: pK_a values of protonation sites

Scheme 1 shows the structure of the two complexes analyzed in this work. In our study of **CoTSC-OCH$_3$** with Et$_3$NH$^+$,[23] calculations showed that HER proceeds via a metal-centered pathway, with the ligand playing mainly the role of electron

relay (Fig. S7†). The reaction under investigation usually proceeding *via* the transfer of two electrons (electrochemical step, E) and two protons (chemical step, C) to form H_2, the catalytic mechanism involving **CoTSC-OCH₃** with Et_3NH^+ was found to be an (E) ECEC-type cycle with the first step (E) being an activation step associated with the release of an axial NCS ligand (Scheme 2).[23] In contrast, HER for **NiTSC-OCH₃** with TFA has a ligand-centered reactivity, with protons and electrons being stored in the ligand (Fig. S8†). In this case, we showed that the catalytic cycle proceeds *via* two pathways, both involving two subsequent proton-coupled electron transfer reactions, [EC][EC]. The difference between these pathways lies with the difference in protonation states, with one of the mechanisms requiring the presence of a third proton, this latter step one being rate-limiting.[24]

Our main question is whether these differences in mechanism are metal-dependent, acid-dependent, or an interplay between both. We first need to review the relative pK_as for protonating the possible sites in both complexes following the methodology used in our previous studies (Tables 2 and 3).[23,24] Four possible sites were considered: M (Ni or Co), S, N_M and N_d (Scheme 2). Other sites were excluded from this analysis based on previous studies.[19] We then performed free energy calculations for the protonated complexes and compared the free energy differences of the distinct protonation states. For the two complexes, with both acids, we are assuming that the complexes have already been reduced once. For **NiTSC-OCH₃**, this is in line with cyclic voltammograms and UV-vis spectra in the presence of TFA,[21] and since TFA is a stronger acid than Et_3NH^+, we would expect the same behavior with the latter. In the case of **CoTSC-OCH₃**, a first reduction step is necessary to activate the complex for the beginning of the catalytic cycle, regardless of the proton source.[20] Thus, for investigating the first protonation event, we are only looking at one-electron reduced species. For **NiTSC-OCH₃**, we are not considering two subsequent reduction events, as those would require larger potentials to be applied (-2.29 *vs.* $Fc^{+/0}$)[24] and the same is true for three subsequent reduction reactions for **CoTSC-OCH₃** (-2.36 V *vs.* $Fc^{+/0}$).[23] Taking this into account, we see that N_d is the most favourable site for protonation for both complexes after a single reduction. Table 3 suggests that the preferred protonation site can become the metal center for **CoTSC-OCH₃**, depend-
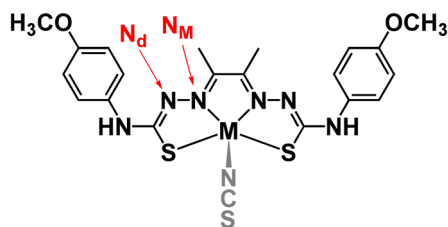
Scheme 2 Structure of the two complexes studied in this work. **M** represents either **Ni** or **Co**, N_M is the N atom coordinated to the metal center, N_d, the distal N atom and NCS the axial ligand in **CoTSC-OCH₃** dissociating after the first reduction.

Table 2 Relative pK_as for the first and second protonation event of **NiTSC-OCH₃** for distinct oxidation states. Due to a break in symmetry from protonating one of the N_d atoms (first protonation), we shall make a distinction between sides **1** and **2** of the complex, in which $N_{d,1}$ is the first protonated site. Results shown for two oxidation states: after the first (1st), and second (2nd) reduction events. Negative results indicate a lesser likelihood of protonation. Results highlighted in grey show the best candidates for protonation. Those marked as '−' with TFA⁻ correspond to unstable protonation states, where the proton moves back to form TFA upon geometry optimization

NiTSC-OCH₃		
Protonated sites	1st	2nd
1st protonation		
N_d	0	—
N_M	−4.2	—
S	−8.2	—
M	−10.8	—
2nd protonation, without TFA⁻		
$N_{d,1}$, $N_{d,2}$	0.0	0.0
$N_{d,1}$ $N_{M,1}$	−6.5	−0.4
$N_{d,1}$ $N_{M,2}$	−10.0	−0.6
$N_{d,1}$ $S_{,1}$	−7.2	−4.1
$N_{d,1}$ $S_{,2}$	−8.7	−4.6
$N_{d,1}$ M	−15.5	−4.3
2nd protonation, with TFA⁻		
$N_{d,1}$, $N_{d,2}$	0	0
$N_{d,1}$ $N_{M,1}$	−2.7	3.1
$N_{d,1}$ M	—	—

Table 3 Relative pK_as for the first, second and third protonation events of **CoTSC-OCH₃** for distinct oxidation states. Due to break in symmetry from protonating one of the N_d atoms (first protonation), we shall make a distinction between sides **1** and **2** of the complex, in which $N_{d,1}$ is the first protonated site. Results shown for two oxidation states: after the first (1st), and second (2nd) reduction events. Negative results indicate lesser likelihood of protonation. Results highlighted in grey show the best candidates for protonation. Those marked as '−' with TFA⁻ correspond to unstable protonation states, where the proton moves back to form TFA upon geometry optimization

CoTSC			
Protonated sites	1st	2nd	3rd
1st protonation			
N_d	0.0	0.0	—
N_M	−19.1	−6.8	—
S	−9.6	−6.8	—
M	−11.1	3.0	—
2nd protonation, without TFA⁻			
$N_{d,1}$, $N_{d,2}$	0.0	0.0	0.0
$N_{d,1}$ $N_{M,1}$	−15.7	−7.3	2.3
$N_{d,1}$ $N_{M,2}$	−24.7	−12.5	2.5
$N_{d,1}$ $S_{,1}$	−16.4	−14.2	−11.9
$N_{d,1}$ $S_{,2}$	−9.9	−7.2	−5.8
M, N_d	−14.8	−0.1	8.5
M, N_M	—	−16.8	0.4
M, S	−8.6	−8.3	0.2
M, M	—	−8.6	13.8
2nd protonation, with TFA⁻			
$N_{d,1}$, $N_{d,2}$	—	0.0	0.0
$N_{d,1}$ $N_{M,1}$	—	−2.5	4.7
$N_{d,1}$ M	—	2.0	7.6
M, N_M	—	—	1.0
M, M	—	−2.5	12.1
3rd protonation, with TFA⁻			
$N_{d,1}$, $N_{M,1}$, $N_{d,2}$	—	—	0.0
$N_{d,1}$, M, $N_{d,2}$	—	—	1.3
$N_{d,1}$, M, $N_{M,1}$	—	−5.8	−2.6
N_d, M, M	—	—	−2.5

ing on the oxidation state of the complex. On the second protonation, it is important to consider the presence of TFA, as a possible double H-bond interaction between this proton source and the complex can take place.

This interaction involves the protonated N_d, the conjugated base TFA$^-$ and either the adjacent protonated N_M atom for **NiTSC-OCH$_3$**,[24] or the metal centre for **CoTSC-OCH$_3$**. Such interaction can affect the pK_as of the adjacent N_M or M atoms. Since it is not the case with Et$_3$NH$^+$, free energy and relative pK_a calculations in the presence of the conjugated base TFA$^-$ were performed only for the stronger proton source. Our results suggest that, for **NiTSC-OCH$_3$** with TFA, protonation could occur either on the second N_d atom or on the N_M atom adjacent to the previously protonated N_d atom. This leads to two possible catalytic pathways, involving two and three protons.[23]

In the case of Et$_3$NH$^+$, Table 2 suggests that we would most likely go through the two-proton mechanism for **NiTSC-OCH$_3$**, with first and second protonation events occurring at both N_d atoms. Thus, the main change in the catalytic mechanism for **NiTSC-OCH$_3$** when considering TFA and Et$_3$NH$^+$ as proton sources lies in the fact that TFA enables a second pathway.

While the complexity in the catalytic mechanism of **NiTSC-OCH$_3$** lies with the possibility of three protons, for **CoTSC-OCH$_3$** we have to consider the transfer of three electrons.[20,23] Previous studies on the HER for **CoTSC-OCH$_3$** with Et$_3$NH$^+$ show that, after an initial reduction step, the cata-

lytic cycle follows an ECEC sequence, with the metal center being the preferred protonation site (Table 3). However, this is the only mechanism available in the presence of Et$_3$NH$^+$. With a stronger acid such as TFA, protonation could occur right after the activation step, and if that is the case, Co is no longer the preferred protonation site, but rather N_d. In the next section, we will show how this order of steps can be changed, leading to distinct pathways being accessed.

DFT calculations: the catalytic cycles

From the data presented in Tables 2 and 3, we can focus the study of the catalytic cycle on the most relevant protonation sites according to the oxidation state of the complexes. Fig. 3 displays the pathways that can be taken for **NiTSC-OCH$_3$** and **CoTSC-OCH$_3$** as function of the proton source strength. We herein report relevant redox potentials, proton transfer free energy differences, as well pK_a differences between the complex and the proton source.

Starting with **NiTSC-OCH$_3$**, since the metal center is unlike to be a proton relay, all the process focuses on the ligand, with the first two protonation events taking place at the N_d atoms, and the third one to the N_M site. The main striking difference between the catalytic cycles for the two proton sources is that TFA can induce proton-coupled electron transfer reactions, whereas for Et$_3$NH$^+$, the cycle undergoes stepwise electron and proton transfers. For TFA, we previously reported that two
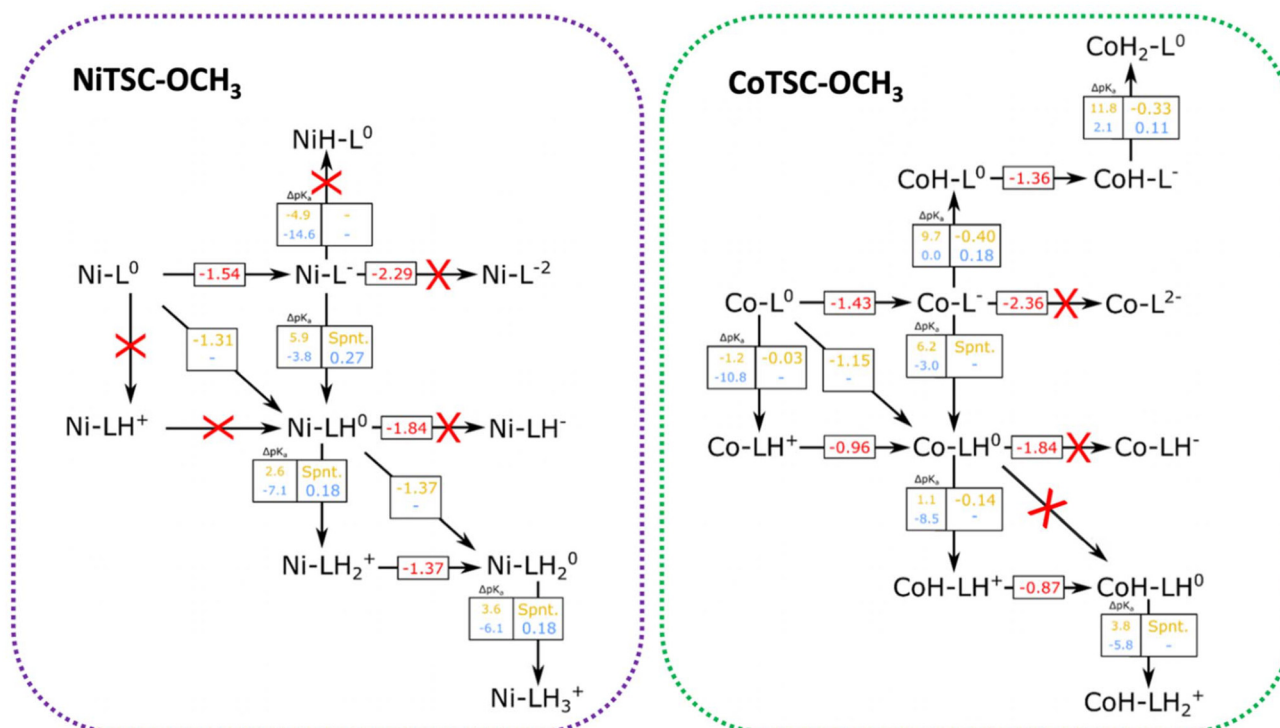
Fig. 3 Possible pathways of HER for **NiTSC-OCH$_3$** and **CoTSC-OCH$_3$**. Protonation is marked as being either on the metal or the ligand, with the specific protonation sites in the ligand determined by Tables 2 and 3. Numbers in red (V vs. Fc$^{+/0}$) correspond to reduction potentials. Numbers in yellow (TFA) and blue (Et$_3$NH$^+$) correspond to pK_a differences between the complexes and the proton source, as well as reaction-free energy differences, all in eV. Red crosses correspond to processes unlikely to occur due to either too negative potential requirements, or large unfavourable pK_a differences (negative numbers are unfavourable).

possible mechanisms were at stake: one involving two protons and two electrons, and another with three protons and two electrons. Both catalytic pathways consisted in two successive PCET providing Ni-LH^0 and NiLH$_2$^{0} and following an [EC][EC] sequence for the first mechanism while the third protonation event involved in the second mechanism provided NiLH$_3$$^+$ following an [EC][EC]C sequence. Particularly for Et$_3$NH$^+$, UV-Vis experiments show that the absence and presence of the proton source does not affect the spectrum (Fig. S6†). This finding suggest that we can discard a mechanism starting with a chemical step (CE and CC) and consider the first part of the cycle being either a stepwise EC process, or a single and concerted [EC] step. As opposed to TFA, our calculations do not predict that a proton-coupled electron transfer is feasible, leaving only the possibility of a reduction as first step (−1.54 V vs. Fc$^{+/0}$) providing NiL$^−$. From there, the arrival of a second electron is unlikely (−2.29 V) while a proton transfer would be able to occur since the ΔpK_a is rather small (−3.8). In this case, such protonation in the presence of Et$_3$NH$^+$ would occur at N$_d$ (Table 2), leading to Ni-LH^0 through a stepwise electron–proton transfer, EC. The second part of the cycle with Et$_3$NH$^+$ is predicted to be a stepwise proton–electron, CE, considering the unfavourable energy requirement for a reduction step following the EC sequence (−1.84 V). In this case, the second protonation would occur at N$_d$ leading the formation of NiLH$_2$$^+$ before a second electron is transferred (−1.37 V) to form the catalytic active species NiLH$_2$^{0}. It is worth noting that pK_a differences between the catalyst and the acid are negative, and reaction free energy differences are substantially positive for all proton transfer events, meaning that the proton transfer reactions are energetically unfavourable, and thus are likely to become rate-limiting steps in the HER process, in contrast with TFA, where the final H$_2$ bond formation is the rate-limiting step. These results thus indicate that the reaction mechanism for **NiTSC-OCH$_3$** with Et$_3$NH$^+$ proceeds through an ECCE sequence.

In the case of **CoTSC-OCH$_3$**, the situation is more complex, especially since the metal center is now playing an active role in the catalytic cycle, holding both protons and electrons. Our previous theoretical study focused on the reaction mechanism of **CoTSC-OCH$_3$** with Et$_3$NH$^+$ showed the catalytic cycle can be best described as a (E) ECEC sequence with a first reduction as the activation step providing CoL^0 and two successive stepwise electron–proton transfers. The first EC steps provided CoL$^−$ and CoH-L^0, while the subsequent EC steps lead to formation of CoH-L$^−$ and CoH$_2$-L^0, respectively. Considering the catalytic cycle of **CoTSC-OCH$_3$** with TFA and CoL^0 as the starting species, either a reduction or a protonation event can occur at this stage. From Fig. 3, we can see that pK_a differences for an early proton transfer are negative regardless of the acid (ΔpK_a = −1.2 and −10.8), meaning that the process is energetically unfavourable. We thus consider that a mechanism starting with a chemical step (CE and CC) is unlikely to occur which points at the first two steps being either an EC or an [EC] process. From CoL^0, a subsequent reduction step predicted at −1.43 V vs. Fc$^{+/0}$ is possible and from there, only a proton transfer would be able to occur. In such case, proton transfer

seems to be feasible with TFA, since the ΔpK_a values are both favorable (9.7 and 6.2, respectively). Such protonation in the presence of TFA could occur either at Co or at N$_d$ (Table 3), providing thus CoH-L^0 and Co-LH^0. It is worth noting that a proton-coupled electron transfer, occurring at −1.15 V and providing Co-LH^0, is also predicted according to our calculations. This reduction process being more than 0.25 eV less negative than in the absence of TFA (−1.43 V), such stabilization effect strongly suggests a PCET phenomenon, just like for **NiTSC-OCH$_3$** with TFA also featuring [EC] as the first steps of the catalytic cycle. A change of similar magnitude in reduction potentials is also observed in the cyclic voltammograms of **CoTSC-OCH$_3$** (Fig. 1) featuring a mid-wave catalytic potential of −1.28 V vs. Fc$^{+/0}$ compared to the 2nd reduction potential of −1.48 V vs. Fc$^{+/0}$ (Table 1). From there, the arrival of a third electron would be unlikely to occur (−1.84 V), meaning the second protonation event would take place at the metal center, in the presence of TFA, providing CoH-LH$^+$ (Table 3). This second proton transfer is energetically favourable and will be followed by a third electron transfer (−0.87 V) providing CoH-LH^0.

The last step would involve a third proton transfer, which, according to Table 3, would leave both N$_d$ and Co protonated providing CoH-LH^{2+}. The three protons are not in optimal distance for H$_2$ bond formation, requiring an intramolecular proton transfer to take place. Table 3 shows that the second-best candidate for the three proton-mechanism would be to have both N$_d$ and one N$_M$ atom protonated, the same protonation pattern seen for **NiTSC-OCH$_3$**, which allows for proton tunneling for H$_2$ formation.[24] The pK_a difference between these two protonation states in **CoTSC-OCH$_3$** is of 1.3, a rather small gap that would not prevent such rearrangement from happening. Our results show that two catalytic pathways can occur for **CoTSC-OCH$_3$** with TFA, involving the transfer of either two or three protons, and proceeding through either [EC]CE or [EC]CEC sequences, respectively.

To summarize, the first steps of the catalytic cycles of both catalysts with Et$_3$NH$^+$ are stepwise electron and proton transfers, EC, but involve different protonation sites e.g. the metal for **CoTSC-OCH$_3$**[23] and the ligand for **NiTSC-OCH$_3$**.[24] Our calculations indicate that the steps following the first EC sequence are different with protonation at the ligand being favored over the reduction for **NiTSC-OCH$_3$**, leading to sequential CE steps, while reduction remains favored over protonation for the cobalt, providing stepwise EC steps. This mechanistic shift is consistent with the previously reported metal-assisted ligand-based reactivity for nickel-based TSC catalysts.[19,24] When comparing the behavior of the two complexes with TFA, a proton-coupled electron transfer, [EC], is the first step of both catalytic cycles. However, the subsequent stepwise proton and electron transfer, CE, occurring for **CoTSC-OCH$_3$** differs from **NiTSC-OCH$_3$** undergoing a second proton-coupled electron transfer, [EC]. Such a change in the reaction pathway is attributed to the metal nature, based on Table 3 which indicates that the cobalt center is a facile protonation site for any investigated redox state. This is also in line with the observed ligand-assisted metal centered-reactivity of the cobalt-based TSC catalyst.[20,23]

The previous section showed that two possible reaction mechanisms can occur concomitantly when using TFA as proton source. One involves two protons and two electrons, while another one requires three protons and two electrons with the transfer of the third proton being the probable rate-limiting steps for both catalysts.[24] For the three proton-mechanism, the relevant nickel and cobalt species display two adjacent N atoms protonated (N_d and N_M), so that two protons are in close proximity for H_2 evolution. In addition, TFA^- is bound by two H-bonds and the second N_d atom is also protonated (Scheme 3). We thus performed a potential energy surface (PES) scan by probing H–H distances in the [2.35–0.75 Å] range and corresponding to values larger than that for complex equilibrium and to H_2 bond length, respectively (Table S4†). The scan was performed by re-optimizing the structure at each point, allowing the remaining atoms to relax while keeping the H···H bond distance constrained.

The calculated PES is presented in Fig. 4. In the [2.35–1.05 Å] range, no noticeable change is observed from the interaction between the two protons, the complexes and the conjugated base TFA^-. The distance between the complex and TFA^- starts increasing when the H–H distance gets shorter leading to the binding of the N_d proton to the adjacent N_M proton. There is an drastic energy drop after the H–H distance reaches 1.10 Å, as H_2 is close to form, and thus dissociates from the complex, together with TFA^-. As previously observed with our series of nickel thiosemicarbazone complexes and other related intramolecular proton transfer processes,[24,36–38] our results provide high activation barriers which would lead to slow reaction rates. In the above cases as well in ours, the energy profiles are rather thin, making tunnelling the main mechanism. We then calculated the rate constant for proton tunneling for the three-proton configuration occurring with TFA, using the PES together with WKB approximation (see details in Experimental section).[23,36–38] The differences in zero-point vibrational energy (ZPVE) between the ground state and the highest energy states were determined through harmonic analysis, which provides the energy at which protons are likely to tunnel through the barrier.

We computed the vibrational frequencies for the two protons (Scheme 3 and Table S4†), specifically for the mode that would bring them together by fitting a parabola to the PES near the equilibrium H–H distance (1.9–2.35 Å).[24] These
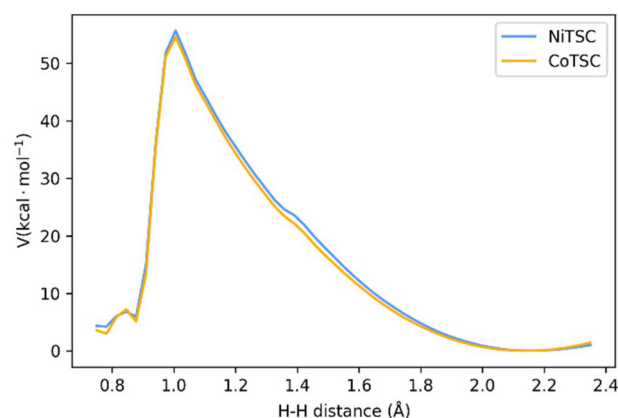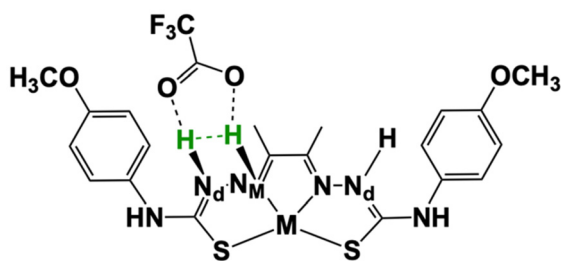

Fig. 4 Potential energy surface scan for the intramolecular proton tunnelling, leading to H_2 formation for the three-proton, two electron mechanisms.

frequencies will indicate the rate at which tunnelling attempts will occur. The tunnelling probability is finally calculated using the WKB approximation,[36–38] and the kinetic rates are derived by multiplying this probability with the calculated frequency of vibration between the two protons. Table 4 compare the kinetics and energetics of the tunneling process for **CoTSC-OCH$_3$** and **NiTSC-OCH$_3$**, showing that **CoTSC-OCH$_3$** would be a better catalyst for this peculiar step. The barrier from the potential energy surface of **CoTSC-OCH$_3$** is slightly thinner and together with a slightly larger zero-point vibrational energy, this leads to a gain of about one order of magnitude in the tunneling rate. These data indicate that there is no apparent correlation between the activation barriers and calculated rates. This aligns with our previous study, where we suggested that the calculated rates resulted from an interplay of all relevant parameters and the contour of the energy barrier.[24] However, we observe a qualitative agreement between the calculated rates and the kinetic experimental data, with the difference in magnitude between the nickel and cobalt catalysts being well reproduced by our calculations. This is consistent with our findings on the series of nickel thiosemicarbazone catalysts for which an agreement was also found from comparing the computed H_2 turnover rates for the three-proton, two-electron mechanism with the experimental TOF values.[24]

Scheme 3 Schematic representation of the intramolecular proton tunnelling coordinate (green labels) used for potential energy surface scan.

Table 4 Comparison between **CoTSC-OCH$_3$** and **NiTSC-OCH$_3$** catalysts for DFT-calculated activation barriers ($\Delta E^{\ddagger}$), zero-point vibrational energy differences between transition and reactant states (ZPVE), vibrational frequencies of protons towards H_2 formation ($\nu(H_2)$), and H_2 turnover rates ($k(H_2)$)

System	$\Delta E^{\ddagger}$ (kcal mol^{-1})	ZPVE (kcal mol^{-1})	$\nu(H_2)$ (cm^{-1})	$k(H_2)$ (s^{-1})
NiTSC-OCH$_3$[a]	55.8	3.3	2341.2	10.8
CoTSC-OCH$_3$	54.7	3.4	2369.5	90.7

[a] Data adapted from ref. 24.

Conclusions

This study provides an in-depth investigation into the HER mechanisms of two metal-based thiosemicarbazone complexes, integrating experimental work with theoretical studies to provide a comprehensive understanding of their catalytic behaviour. Our results confirm that the strength of the proton source significantly influences the reaction pathways, with the stronger proton source, TFA, favouring a proton-coupled electron transfer (PCET) as the dominant initial step in the catalytic process for both catalysts. This finding is in sharp contrast with the step-by-step reduction and protonation events that predominate when using a weaker proton source, such as Et_3NH^+. We also showed the existence of two competing mechanisms with TFA, involving two electrons and either two or three protons while a single reaction pathway was identified with Et_3NH^+. Irrespective of the proton source, our calculations identified mechanistic shifts between the catalysts following the first electron–proton transfers that were attributed to the metal-centered reactivity of **CoTSC-OCH₃** as opposed to the ligand-centered one for **NiTSC-OCH₃**. Part of these mechanistic distinctions align with previous findings reported by the group of Artero who highlighted the gap in understanding how acid strength impacted the mechanism of cobalt-based complexes for HER.[14] Their work identified distinct catalytic pathways, with either stepwise or concerted events, featuring different hydride intermediates. Isolating the latter can be challenging, which complicates further characterization. As a result, the complete sequence of steps leading to hydrogen release remains elusive when relying solely on experimental approaches. In this context, theoretical studies can provide a detailed framework for analyzing the pivotal role of proton source strength in shaping the reaction mechanism. In this study, DFT calculations allowed to propose plausible reaction pathways, pinpoint key intermediates, and identify potential rate-limiting steps within the catalytic cycle. The computed values derived from these calculations could be further compared with experimental data, providing valuable insights into the HER mechanism. For instance, our calculations indicated that the PCET process is energetically less demanding compared to the stepwise process which nicely correlates with the lower overpotential requirements of both complexes when using the stronger proton source. Our results also revealed the presence of two catalytic pathways with the stronger proton source which can be correlated to prolonged HER activity of the catalysts with TFA when compared to that with Et_3NH^+. Our computations also indicated the favorable formation of reactive hydride species with the cobalt catalyst which can be ascribed with the enhanced catalytic efficiency of **CoTSC-OCH₃** compared to **NiTSC-OCH₃** with both proton sources at early-stage catalysis. From the above correlations, our study lays the groundwork for future research targeting the design of next-generation metal-based HER catalysts with redox-active ligands. Our findings suggest the preferential use of cobalt systems with softer proton sources to enhance catalyst activity and efficiency. By improving our mechanistic understanding

of thiosemicarbazone metal-based complexes for HER, this study highlights the potential of a multidisciplinary approach to accelerate the optimization of catalytic systems.

Experimental section

All chemical compounds were purchased from Sigma Aldrich and used without further purification. UV-vis spectra were recorded on a Varian Cary 60 spectrophotometer.

Cyclic voltammetry experiments were performed using an Origaflex OGF01A potentiostat and a three-electrode set-up consisting of a glassy carbon working electrode, a platinum wire counter electrode and a Leakless (Ag/AgCl) reference electrode. Ferrocene was used as an internal standard with $E°$ (Fc$^{+/0}$) = 0.5 V *versus* Ag/AgCl for each measurement. All studies were performed in deoxygenated DMF containing NBu_4PF_6 (0.1 M) as supporting electrolyte. Controlled potential electrolysis experiments were carried out in a two-compartment cell. The volume of solution (DMF, 0.1 M NBu_4PF_6) used in the working compartment of the cell was 8 mL. The working electrode used was a pool of mercury, separated from the coiled platinum wire counter electrode by a porous frit. Bulk electrolysis solutions were purged with N_2 gas for at least 1 hour prior to electrolysis and stirred throughout bulk electrolysis experiment. During the experiment, the cell was continuously purged with nitrogen (5 mL min⁻¹) and the output gas was analysed at ten-minute intervals in a Shimadzu GC-2010 pro gas chromatographer.

DFT calculations

We used the same computational protocol from out previous studies.[23,24] Calculations were performed with the ORCA program package,[28,29] with BP86/def2-TZVP(-f) as our level of theory.[30–33] Following ORCA's convention, we used 'Grid4' and 'TightSCF' as our integration grid and convergence criteria. Solvent effects from DMF were included *via* CPCM.[34] Free energy differences were obtained from numerical frequencies calculations (NumFreq in ORCA). We obtained the Gibbs free energy difference for the ferrocene reduction in DMF, to allow for direct comparison of reduction potentials reported experimentally against such reference, with $\Delta G(Fc^{+/0})$ = 4.87 eV. We used Chemcraft to create images for the 3D chemical structures and orbitals.[35]

Tunneling calculations

We used the WKB approximation to obtain approximate reaction rates for H_2 formation.[36–38] The probability of tunnelling is given by:

$$T(E) = \exp\left[-2\int_a^b \frac{2(2m_p)}{\hbar}[V(x) - E]dx\right]$$

where a and b are the initial and final H–H distances for the protons to tunnel from one well to another of the PES. This interval is determined based on zero-point vibration energy differences between the ground and transition states of the

proton tunnelling PES, which give an offset to the ground state, reflecting the vibration of the protons following the transfer through the PES. We calculated the difference between the ground and highest-energy states. As previously reported for **NiTSC-OCH₃**,[24] we took the highest-energy state as an approximation to the transition state. Although it possessed two imaginary frequencies, both are associated with the proton vibrations, as well as with the movement of TFA⁻. In the equation, V is the potential energy, E is the ground state energy, which includes ZPVE, and m_p is the mass of the proton. We are considering twice the mass since both protons are attempting tunnelling through the barrier at once. To perform the PES, we took 33 points for distinct H–H distances, from 2.35 Å to 0.75 Å with intervals of 0.05 Å in between. Finally, the PES curve is obtained using a cubic spline, and the integral is solved numerically using the Fortran library QUADPACK, as implemented in the SciPy library.

Author contributions

J. M., L. D. and M. P. carried out the experimental work and A. B. carried out the theoretical calculations. R. H., M. P. and M. O. analysed and interpreted the experimental and theoretical data. M. O. conceived and designed the project. M. P. and M. O. prepared the manuscript. All authors reviewed and contributed to the manuscript.

Data availability

The data supporting this article have been included as part of the ESI.†

Crystallographic data for **NiTSC-OCH₃** and **CoTSC-OCH₃** are deposited at the CCDC 1497214 and 1576527, respectively and can be obtained from https://www.ccdc.cam.ac.uk/.

Conflicts of interest

There are no conflicts to declare.

Acknowledgements

References

1 J. C. Fontecilla-Camps, A. Volbeda, C. Cavazza and Y. Nicolet, *Chem. Rev.*, 2007, **107**, 4273–4303.

2 K. A. Vincent, A. Parkin and F. A. Armstrong, *Chem. Rev.*, 2007, **107**, 4366–4413.

3 W. Lubitz, H. Ogata, O. Rüdiger and E. Reijerse, *Chem. Rev.*, 2014, **114**, 4081–4148.

4 M. L. Helm, M. P. Stewart, R. M. Bullock, M. R. DuBois and D. L. DuBois, *Science*, 2011, **333**, 863–866.

5 M. Y. Darensbourg, E. J. Lyon and J. J. Smee, *Coord. Chem. Rev.*, 2000, **206–207**, 533–561.

6 T. B. Rauchfuss, *Acc. Chem. Res.*, 2015, **48**, 2107–2116.

7 Z. Li, Y. Ohki and K. Tatsumi, *J. Am. Chem. Soc.*, 2005, **127**, 8950–8951.

8 K. Weber, T. Krämer, H. S. Shafaat, T. Weyhermüller, E. Bill, M. Van Gastel, F. Neese and W. Lubitz, *J. Am. Chem. Soc.*, 2012, **134**, 20745–20755.

9 D. Brazzolotto, M. Gennari, N. Queyriaux, T. R. Simmons, J. Pécaut, S. Demeshko, F. Meyer, M. Orio, V. Artero and C. Duboc, *Nat. Chem.*, 2016, **8**, 1054–1060.

10 H. I. Karunadasa, C. J. Chang and J. R. Long, *Nature*, 2010, **464**, 1329–1333.

11 M. Razavet, V. Artero and M. Fontecave.

12 P. Zhang, M. Wang, Y. Yang, T. Yao and L. Sun, *Angew. Chem., Int. Ed.*, 2014, **53**, 13803–13807.

13 E. J. Thompson and L. A. Berben, *Angew. Chem., Int. Ed.*, 2015, **54**, 11642–11646.

14 N. Queyriaux, D. Sun, J. Fize, J. Pécaut, M. J. Field, M. Chavarot-Kerlidou and V. Artero, *J. Am. Chem. Soc.*, 2020, **142**, 274–282.

15 X. Jing, P. Wu, X. Liu, L. Yang, C. He and C. Duan, *New J. Chem.*, 2015, **39**, 1051–1059.

16 C. F. Wise, D. Liu, K. J. Mayer, P. M. Crossland, C. L. Hartley and W. R. McNamara, *Dalton Trans.*, 2015, **44**, 14265–14271.

17 A. Z. Haddad, B. D. Garabato, P. M. Kozlowski, R. M. Buchanan and C. A. Grapperhaus, *J. Am. Chem. Soc.*, 2016, **138**, 7844–7847.

18 A. Z. Haddad, S. P. Cronin, M. S. Mashuta, R. M. Buchanan and C. A. Grapperhaus, *Inorg. Chem.*, 2017, **56**, 11254–11265.

19 T. Straistari, J. Fize, S. Shova, M. Réglier, V. Artero and M. Orio, *ChemCatChem*, 2017, **9**, 2262–2268.

20 T. Straistari, R. Hardré, J. Fize, S. Shova, M. Giorgi, M. Réglier, V. Artero and M. Orio, *Chem. – Eur. J.*, 2018, **24**, 8779–8786.

21 M. Papadakis, A. Barrozo, T. Straistari, N. Queyriaux, A. Putri, J. Fize, M. Giorgi, M. Réglier, J. Massin, R. Hardré and M. Orio, *Dalton Trans.*, 2020, **49**, 5064–5073.

22 M. Papadakis, J. Mehrez, I. Wehrung, L. Delmotte, M. Giorgi, R. Hardré and M. Orio, *ChemCatChem*, 2024, e202400426.

23 A. Barrozo and M. Orio, *ChemPhysChem*, 2022, **23**, e202200056.

24 A. Barrozo and M. Orio, *RSC Adv.*, 2021, **11**, 5232–5238.

25 M. Papadakis, G. Landrou, M. Poisson, L. Delmotte, K. Achileos, S. Bertaina, R. Hardré, K. Ladomenou, A. G. Coutsolelos and M. Orio, *Eur. J. Inorg. Chem.*, 2023, **26**, e202300352.

26 B. D. McCarthy, D. J. Martin, E. S. Rountree, A. C. Ullman and J. L. Dempsey, *Inorg. Chem.*, 2014, **53**, 8350–8361.

27 V. Fourmond, P.-A. Jacques, M. Fontecave and V. Artero, *Inorg. Chem.*, 2010, **49**, 10338–10347.

28 F. Neese, *Wiley Interdiscip. Rev.: Comput. Mol. Sci.*, 2012, **2**, 73–78.

29 F. Neese, *Wiley Interdiscip. Rev.: Comput. Mol. Sci.*, 2018, **8**, e1327.

30 J. P. Perdew, *Phys. Rev. B: Condens. Matter Mater. Phys.*, 1986, **33**, 8822–8824.

31 J. P. Perdew, *Phys. Rev. B:Condens. Matter Mater. Phys.*, 1986, **34**, 7406–7406.

32 A. D. Becke, *Phys. Rev. A: At., Mol., Opt. Phys.*, 1988, **38**, 3098–3100.

33 A. Schäfer, C. Huber and R. Ahlrichs, *J. Chem. Phys.*, 1994, **100**, 5829–5835.

34 V. Barone and M. Cossi, *J. Phys. Chem. A*, 1998, **102**, 1995–2001.

35 Chemcraft – Graphical software for visualization of quantum chemistry computations, **https://www.chemcraft-prog.com**.

36 P. R. Schreiner, H. P. Reisenauer, D. Ley, D. Gerbig, C.-H. Wu and W. D. Allen, *Science*, 2011, **332**, 1300–1303.

37 M. Schäfer, K. Peckelsen, M. Paul, J. Martens, J. Oomens, G. Berden, A. Berkessel and A. J. H. M. Meijer, *J. Am. Chem. Soc.*, 2017, **139**, 5779–5786.

38 H. Quanz and P. R. Schreiner, *J. Comput. Chem.*, 2019, **40**, 543–547.